Research Article

Enhanced selective adsorption ability of Cu_2O nanoparticles for anionic dye by sulfur incorporation

Jiaxing Sun[1] · Tao Song[1] · Junwen Wang[1] · Xiangyu Guo[1] · Lei Su[1] · Weixia Tu[1]

Received: 13 April 2020 / Accepted: 15 May 2020 / Published online: 21 May 2020

Abstract
Cu_2O-based materials are potential adsorbents for the removal of anionic dyes pollutions. Herein, sulfur incorporation is designed to promote adsorption capacity of Cu_2O. A series of sulfur-incorporated Cu_2O nanomaterials are synthesized by a facile chemical reduction method. Sulfur incorporation favors the formation of small sized S-Cu_2O particles in the range of 50–100 nm and their enhanced adsorption performances. The S-Cu_2O particles show good adsorption activities for methyl orange solution (75–500 mg L^{-1}) under pH 6–10 at room temperature. A superior adsorption capacity of 1485.24 mg g^{-1} for the removal of methyl orange is achieved on the S-Cu_2O adsorbent. Adsorption behaviors of the S-Cu_2O adsorbent fit well with Langmuir isotherm and pseudo-second-order kinetic model. Adsorption thermodynamic results indicate the exothermic and spontaneous adsorption process. Anionic dye can be adsorbed selectively on the S-Cu_2O adsorbent and separated from cationic dyes. Density functional theory calculations prove a pronounced electron accumulation on sulfur sites, benefiting to the adsorption on S-Cu_2O. A nonmetallic element incorporation for improving adsorption capacity of metal oxide adsorbents is provided as a promising strategy for other adsorbents.

Keywords Adsorption · Cu_2O · Nonmetallic element · Sulfur incorporation · Anionic dye

1 Introduction

With the industrialization development, organic dyes have been widely used in industries, such as textiles, rubber, paper, medicine, etc. [1]. Water pollutions containing dyes have become serious environmental problems due to their high toxicity, mutagenicity and carcinogenicity [2]. To date, various technologies for the removal of dyes from water have been explored, including coagulation [3], membrane separation [4], photocatalysis [5] and adsorption [6]. Among them, adsorption technology is considered to be efficient and economical because of its simplicity and low cost [7, 8]. Various adsorbents including porous structure materials, biomass materials, metals or metal oxides have been used for the removal of dyes [9–12]. To explore new adsorbents with high efficiency is still essential for removing dyes pollutions in practical applications.

Among dyes pollutants, reactive azo dyes are widely used in many industries. These azo dyes contain one or more azo groups with heterocyclic and aromatic rings accompanying with sulfonates or chloride functional groups. Low biodegradability of the azo groups presents serious environmental risks [13–16]. Methyl orange (MO) is a typical acidic anionic mono-azo dye, which is usually selected as a test anionic dye for performance studies of new adsorbents. To date, various materials have been studied as adsorbents for the removal of MO, such as clay [17], carbon-based materials [18],

Electronic supplementary material The online version of this article (https://doi.org/10.1007/s42452-020-2914-x) contains supplementary material, which is available to authorized users.

✉ Weixia Tu, tuwx@mail.buct.edu.cn | [1]State Key Laboratory of Organic-Inorganic Composites, College of Chemical Engineering, Beijing University of Chemical Technology, Beijing 100029, People's Republic of China.

chitosan [19], polyaniline (PANI) [20–22], layered double hydroxide-base materials (LDHs) [23], metal–organic frameworks (MOFs) [24] and metal oxides (Zn, Fe) [25–27]. Wherein, cuprous oxide (Cu_2O) has attained much attention in the adsorption of dyes. A variety of cuprous oxide nanostructures including nanospheres, octahedral nanoparticles and nanocubes have been synthesized and used as potential adsorbents for the removal of organic dyes in waste water. Porous Cu_2O spheres around 400 nm had the adsorption capacity of 47.5 $mg{\cdot}g^{-1}$ for MO [28]. Octahedral shaped Cu_2O particles were reported with a adsorption capacity of 96.42 mg g^{-1} [29]. Cu_2O hollow nanospheres in diameter around 60–110 nm showed a maximum capacity of 297.62 mg g^{-1} for MO [30]. Novel uniform Cu_2O nanocrystals with average size of 4 nm were suitable for the adsorption of MO with an amount of 366.78 mg g^{-1} [31]. Besides the above monocomponent adsorbents, Cu_2O was composited with other metals or metal oxides in order to increase its adsorption performance. Kou et al. [32] provided nanoporous core–shell Cu@Cu_2O with adsorption capacity of 344.84 mg g^{-1} for MO. Sasmal et al. [33] reported hybrid Cu_2O–Ag bearing a high adsorption capacity of 501.23 mg g^{-1}. Nanoparticles-assembled mesoporous Cu_2O/Bi_2O_3 [34] showed a maximum adsorption amount of 1533.2 mg g^{-1}. Clearly, Cu_2O is a kind of suitable adsorbent for adsorption of MO, and the added metallic components in Cu_2O composites would promote their adsorption capacities. However, nonmetallic element-incorporated Cu_2O was rarely reported [35] and its adsorption performance has not been concerned till now.

In this work, nonmetallic element sulfur-incorporated Cu_2O (S-Cu_2O) was synthesized via a facile method and effect of sulfur incorporation was investigated on the adsorption removal of organic dye MO. Structure characterizations using scanning electron microscope, high-resolution transmission electron microscope, X-ray powder diffractometer and X-ray photoelectron spectroscopy were involved to verify the formation of sulfur-incorporated Cu_2O. Adsorption behaviors of the S-Cu_2O for MO were investigated through adsorption kinetic studies, adsorption isotherms and thermodynamic analysis. The selective adsorption abilities of S-Cu_2O were evaluated for anionic dye separated from cationic dyes. Adsorption interaction was discussed based on Fourier transform infrared spectroscopy characterizations. The promotion effect of sulfur incorporation was analyzed through density functional theory calculations. A simple and promising way through nonmetallic element incorporation is provided for enhancing adsorption performance of metal oxide adsorbents.

2 Experimental

2.1 Materials

Polyvinylpyrrolidone (PVP K-30) and ascorbic acid (AA) were purchased from Beijing Tongguang Fine Chemicals Company. Cupric chloride dihydrate ($CuCl_2{\cdot}2H_2O$) was supplied by the Tianjin Yongda Chemical Reagent Company Limited. Thioacetamide (TAA) was gained from Shanghai Macklin Biochemical Co. Ltd. Sodium hydroxide (NaOH) was provided by Shanghai Aladdin Biochemical Technology Co. Ltd. Ammonium hydroxide ($NH_3{\cdot}H_2O$, 25%) and methyl orange (MO) were got from Beijing Chemical Works. Methylene blue (MB) was purchased from Adamas Reagent Co., Ltd. Crystal violet (CV) was obtained from Tianjin FuChen Chemical Reagents Factory. All the reagents were analytical grade and used as received without any further purification.

2.2 Synthesis of sulfur-incorporated Cu_2O adsorbents

Sulfur-incorporated Cu_2O materials were synthesized through a facile liquid-phase reduction method. Typically, $CuCl_2{\cdot}2H_2O$ (0.68 g) and PVP (3.0 g) were mixed in 100 mL of deionized water and the mixture was kept at 55 °C under a water bath. Then, 20 mL of NaOH (6 mol L^{-1}) and 3.9 mL of $NH_3{\cdot}H_2O$ were slowly added with continuous stirring for 15 min. TAA aqueous (5 mL with a certain concentration) was added successively keeping stirring for 15 min. Finally, 20 mL of AA (1.2 mol L^{-1}) as reducing agent was dropped into the above mixture. After stirring for 3 h, the resulting product was collected by centrifugation and washed with deionized water and anhydrous ethanol. The as-prepared samples were dried at 60 °C in a vacuum oven for 12 h. Sulfur-incorporated Cu_2O materials with different sulfur incorporation were prepared by adjusting molar percentage of TAA to $CuCl_2$ (TAA: $CuCl_2$ = 2.5%, 15%, 30%, 37.5% and 100%) under the same synthesis conditions, which were named as $S_{2.5\%}$-Cu_2O, $S_{15\%}$-Cu_2O, $S_{30\%}$-Cu_2O, $S_{37.5\%}$-Cu_2O and $S_{100\%}$-Cu_2O, respectively. Pure Cu_2O without sulfur incorporation was prepared without adding TAA and the obtained sample was labeled as Cu_2O.

2.3 Characterization

X-ray powder diffractometer (XRD, Brucker D8-Advance, Germany) with a scan step of 0.02° and scan range between 10° and 90° was used for acquiring the crystallinity and component information of materials. Scanning electron microscope (SEM) images were taken on an S-4700F instrument

(Japan JEOL Ltd.). High-resolution transmission electron microscope (HR-TEM) images were collected on a J-3010 microscope (Japan JEOL Ltd.) with energy dispersive X-ray spectroscopy (EDX). X-ray photoelectron spectroscopy (XPS) measurement was taken using an ultrahigh vacuum VG ESCALAB-250 electron spectrometer. The Fourier transform infrared (FT-IR) spectroscopy was measured by Nicolet 8700 spectrometry using KBr pellets. Inductively coupled plasma spectrometry-atomic emission spectrometer (ICP-AES, ULTIMA, JY Inc.) was operated to characterize the chemical compositions of the sample.

2.4 Adsorption experiments

Adsorption capacities of the synthesized S-Cu_2O materials were evaluated on removal of MO from aqueous solution. Typical adsorption test was carried out as following: 10 mg of S-Cu_2O adsorbent was immersed into 100 mL of MO solution under constant stirring for 24 h at room temperature. The initial concentration of MO aqueous solution was 75, 150, 200, 300, 400, 500 mg L^{-1}, respectively. 1 mL of suspension was taken out at different interval and was filtered using a 0.22 μm microporous membrane filter to get clear liquor. The maximum absorbance of the liquor was determined under UV–Vis spectrophotometer (TU-1901, Beijing, China) at wavelength of 464 nm. According to standard calibration curve of standard dye concentration and the corresponding absorbance, concentration of remaining dye without adsorption was calculated. The equilibrium adsorption capacity (q_e) was calculated according to the following Eq. (1):

$$q_e = \frac{V(C_0 - C_e)}{W} \quad (1)$$

where q_e (mg g^{-1}) is equilibrium adsorption amount; C_0 and C_e (mg L^{-1}) are initial and equilibrium concentrations of MO, respectively; V (L) is volume of dye solution; and W is weight of the added adsorbent. Adsorption reaction was performed under different pH and temperature in the dark for 24 h. pH of the solution was adjusted in the range of 7–11 by buffer solutions. Temperature was increased from 298 to 313 K. For adsorption kinetics, 10 mg of adsorbent was dispersed into 100 mL of the MO solution (150 mg L^{-1}). The remaining concentration of MO was determined after different interval adsorption.

3 Results and discussion

3.1 Characterization of the S-Cu_2O nanomaterials

Several sulfur-incorporated Cu_2O nanomaterials through adjusting amount of sulfur precursor were synthesized by a facile chemical reduction method. Figure 1 shows XRD patterns of S-Cu_2O nanomaterials and pure Cu_2O for comparison. Characteristic peaks for the S-Cu_2O materials ($S_{2.5\%}$-Cu_2O, $S_{15\%}$-Cu_2O, $S_{30\%}$-Cu_2O, $S_{37.5\%}$-Cu_2O) in Fig. 1 were similar to pure Cu_2O without S, which was indexed to a pure cubic phase of Cu_2O (PDF#34-1354). The diffraction peaks with 2θ values of 29.63°, 36.63°, 42.57°, 61.81°, 74.05° and 77.41° corresponded to (110), (111), (200), (220), (311) and (222) crystal planes, respectively. These sharp peaks confirmed high crystallinity of S-Cu_2O as pure Cu_2O. Because of the low content of incorporated sulfur, no additional peak was detected. Evidently, the visible peak shifts in the inset of Fig. 1 indicated the successive element incorporation in Cu_2O. The incorporated sulfur resulted in the increase of the distance between adjacent lattice planes due to the larger atom radius of sulfur than oxygen. Based on the Bragg's low, the peaks would shift to small angle as illustrated in the inset [36, 37]. For the $S_{100\%}$-Cu_2O sample given in Fig. S1, its XRD characteristic peaks were different quietly, which indicated the formation of Cu_7S_4 other than Cu_2O due to the large amount of TAA used in the synthesis.

SEM images of pure Cu_2O and S-Cu_2O nanomaterials are given in Fig. 2a–d. All these materials contained homogeneous cubic particles. Particles sizes of pure Cu_2O were around 1.5 μm. With the sulfur incorporation, morphologies of S-Cu_2O were unchanged as cubic similar to pure

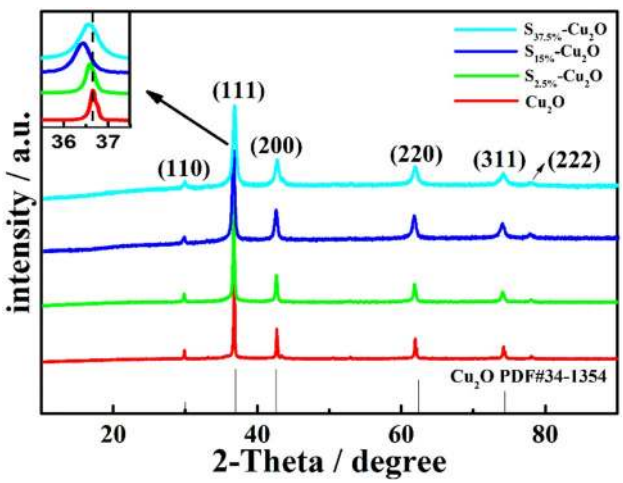

Fig. 1 XRD patterns of the synthesized S-Cu_2O and Cu_2O nanomaterials

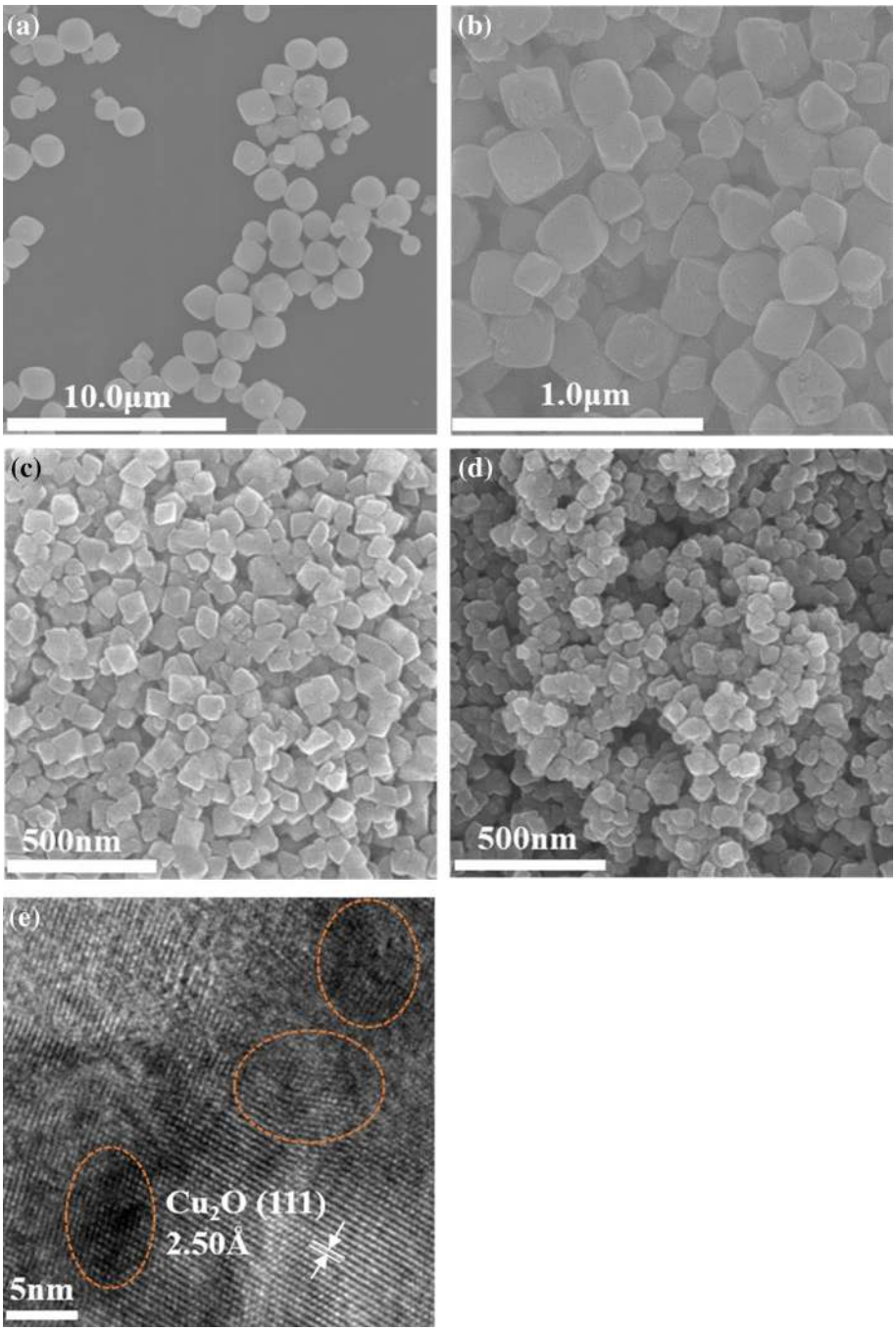

Fig. 2 SEM images of the synthesized S-Cu_2O and Cu_2O nanomaterials: **a** pure Cu_2O; **b** $S_{2.5\%}$-Cu_2O; **c** $S_{15\%}$-Cu_2O and **d** $S_{37.5\%}$-Cu_2O; **e** HR-TEM image of $S_{15\%}$-Cu_2O

Cu_2O, while particles sizes of them decreased greatly. The more sulfur precursor added, the smaller particles formed. Particles sizes of $S_{2.5\%}$-Cu_2O, $S_{15\%}$-Cu_2O, $S_{37.5\%}$-Cu_2O were around 200, 100, 50 nm, respectively. HR-TEM image of $S_{15\%}$-Cu_2O in Fig. 2d indicated the lattice spacing of 2.50 Å well matched with (111) crystal planes of Cu_2O. Due to the incorporation of sulfur, the disordered lattice fringes and defect sites formed and were found in some regions marked with yellow circles. The crystal structure defects as a result of the sulfur incorporation would act as a barrier to restrict the crystal growth causing the reduced particle size [38, 39]. From EDX and ICP analyses results of $S_{15\%}$-Cu_2O, the molar percentage of S/Cu was calculated to be 2.9% and 2.7%, respectively, which was less than that of the staring reactants (15% TAA/Cu).

XPS characterization of $S_{15\%}$-Cu_2O was performed to investigate chemical states. Figure 3 gives high resolution XPS spectra of Cu, O and S elements. Binding energy scales were referenced by setting the C 1*s* BE as 284.8 eV. Through Gaussian fitting analysis, spectra of Cu in Fig. 3a

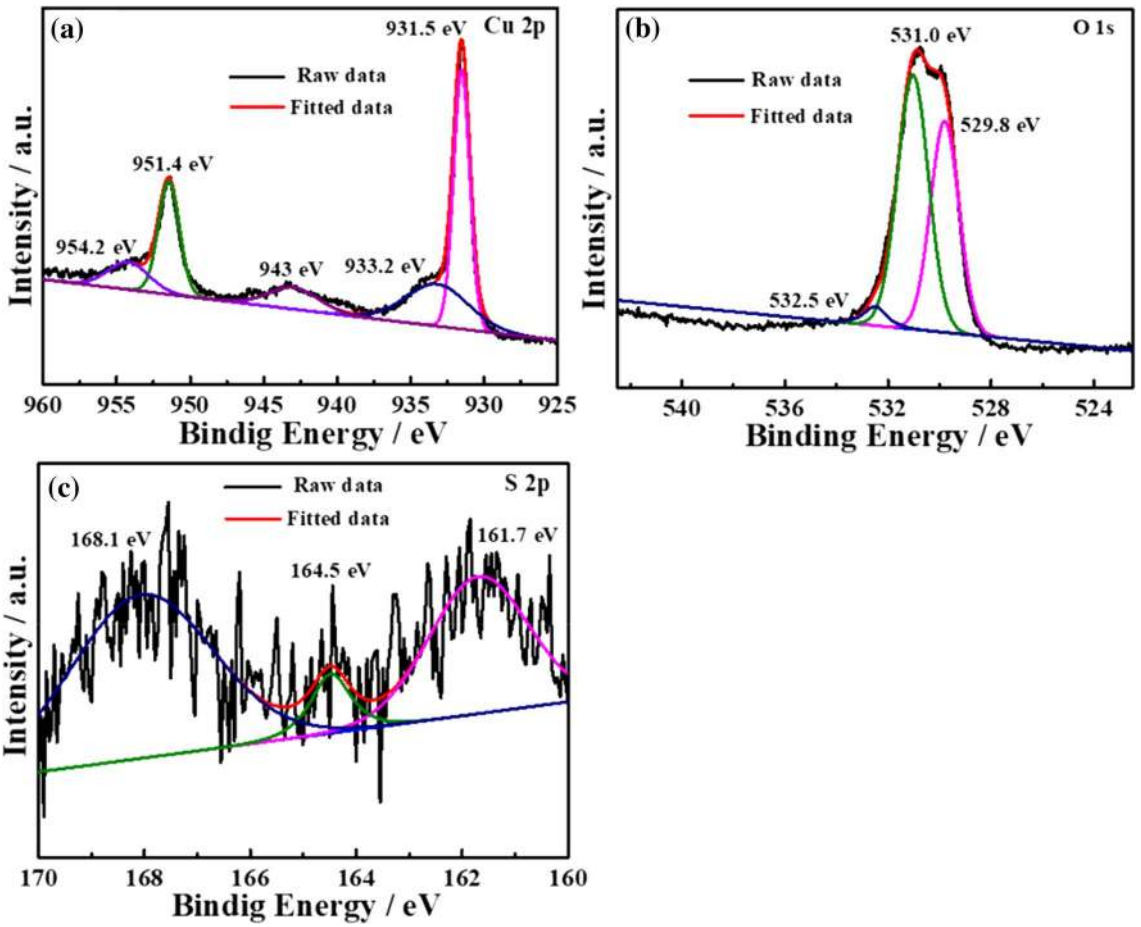

Fig. 3 High resolution XPS spectra of $S_{15\%}$-Cu_2O: **a** Cu 2*p*; **b** O 1*s*; **c** S 2*p*

could be well fitted with two spin–orbit doublets peaks as well as one shakeup satellite peak. Two strong peaks with binding energies located at 931.5 eV and 951.4 eV were assigned to Cu $2p_{3/2}$ and Cu $2p_{1/2}$ of Cu^+ in Cu_2O [40]. Two weak peaks at 933.2 eV and 954.2 eV were attributed to Cu^{2+}. The existence of trace Cu^{2+} might due to the oxidation of Cu_2O to CuO during the preparation process [41]. The satellite peak of Cu centered at binding energy of 943.0 eV could be observed when the outgoing photoelectrons simultaneously interact with a valence electron and excite to a higher energy level [42]. The O 1*s* spectra shown in Fig. 3b could be divided into three peaks at 529.8 eV, 531.0 eV and 532.5 eV through Gaussian fitting, which would be ascribed to lattice oxygen in Cu_2O, the presence of hydroxyl groups and adsorbed oxygen on the surface of the S-Cu_2O [43]. Illustrated S 2*p* spectra in Fig. 3c showed several components in the S-Cu_2O. The peak at 161.7 eV was consistent with sulfur ion (S^{2-}), the peaks at 164.5 eV and 168.1 eV could be ascribed to oxysulfide and sulfate [44]. The results revealed that the incorporated sulfur presented partially as oxidized states.

3.2 Adsorption capacity of the S-Cu_2O nanomaterials

The sulfur-incorporated Cu_2O nanomaterials were investigated as adsorbents for the removal of anionic dye MO. Their adsorption capacities were compared with pure Cu_2O to understand effect of sulfur incorporation. Figure 4a displays equilibrium adsorption capacity of S-Cu_2O adsorbents in 150 mg L^{-1} of MO solution. Obviously, the present pure Cu_2O showed good adsorption ability with 530.93 mg g^{-1}, which was higher than most of reported Cu_2O adsorbents [28–31, 45]. A suitable incorporation of sulfur was effective to enhance adsorption capacity of Cu_2O. Among the adsorbents, $S_{15\%}$-Cu_2O exhibited the highest adsorption capacity with 954.69 mg g^{-1}. Based on the XRD results of the inset in Fig. 1, the visible peak shift of the $S_{15\%}$-Cu_2O adsorbent is largest indicating the suitable incorporation of sulfur in Cu_2O for the highest adsorption capacity. The following contents focused on the adsorption performance of $S_{15\%}$-Cu_2O.

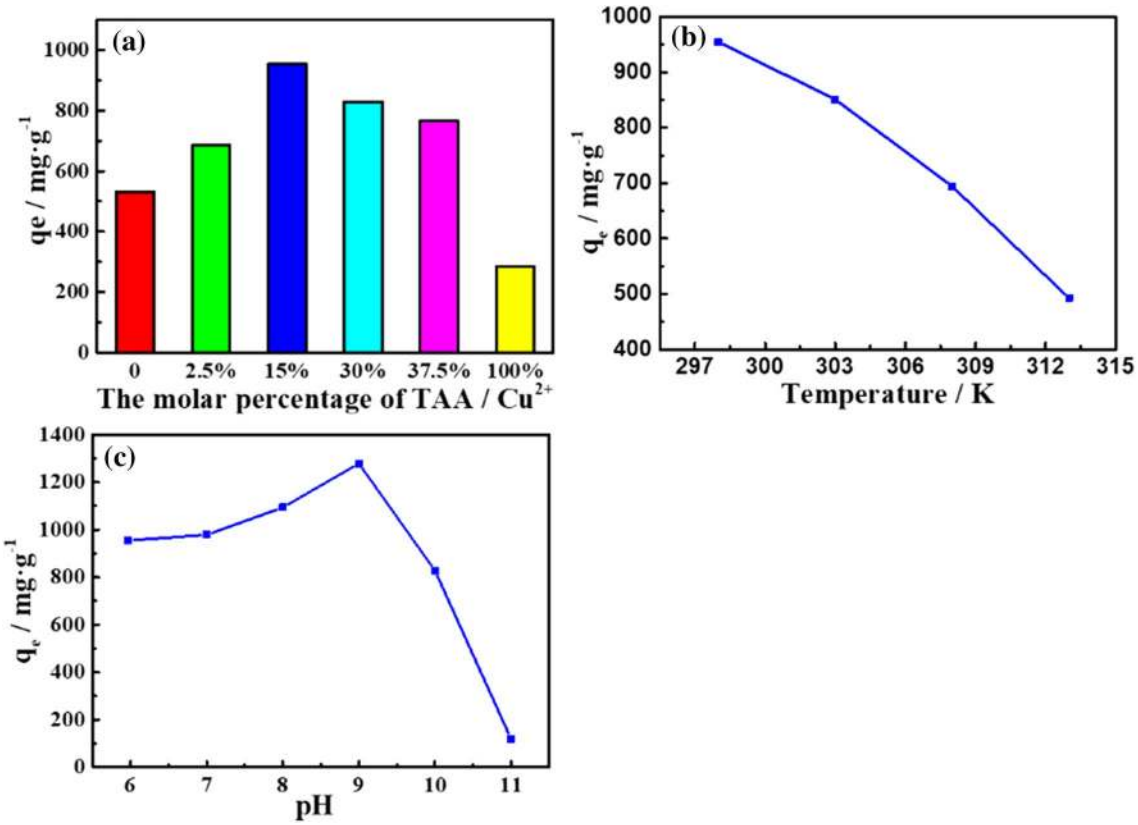

Fig. 4 **a** Adsorption performances of different S-Cu_2O adsorbents for MO; effect of **b** temperature and **c** pH on the adsorption capacity of $S_{15\%}$-Cu_2O

Temperature and pH are important parameters affecting adsorption process. Adsorption activity was evaluated under different temperature and pH. Batch adsorption experiments were performed on $S_{15\%}$-Cu_2O at different temperatures in the range of 298–313 K. The adsorption capacity results are displayed in Fig. 4b. The decreased adsorption capacities with the increasing temperature indicated that the adsorption process was exothermic. Room temperature at 298 K was chosen for the following experiments which was beneficial to the adsorption removal of MO on $S_{15\%}$-Cu_2O. Figure 4c shows adsorption capacities of $S_{15\%}$-Cu_2O under different pH conditions. Without pH adjustment, MO solution with $S_{15\%}$-Cu_2O adsorbent has the pH value of 6, and the adsorption capacity was 954.69 mg g^{-1}. Under the acidic solution, the adsorbent was unstable and would be dissolved. So, adsorption capacity of $S_{15\%}$-Cu_2O varied with pH in the range of 7–11. While the pH increased from 7 to 9, the adsorption amounts of MO increased from 978.36 to 1278.68 mg g^{-1}. With further increase of pH to be 11, the adsorption amount decreased to 117.97 mg g^{-1}, which may be due to the excessive hydroxyl ions competing with the adsorbent.

3.3 Adsorption kinetic studies

To investigate adsorption behavior of MO on the $S_{15\%}$-Cu_2O adsorbent, adsorption kinetic studies were carried out at different adsorption contact time. 10 mg of the adsorbent was mixed in MO solution (150 mg L^{-1}, 100 mL). Herein, pseudo-first-order, pseudo-second-order and Weber's intraparticle diffusion models [46] were applied to describe the adsorption dynamics process. The linearized integral forms of pseudo-first-order, pseudo-second-order and Weber's intraparticle diffusion models are presented as following equations:

$$\text{Pseudo - first - order kinetic model:} \quad \ln\left(q_e - q_t\right) = \ln q_e - k_1 t \tag{2}$$

$$\text{Pseudo - second - order kinetic model:} \quad \frac{t}{q_t} = \frac{1}{q_e^2 k_2} + \frac{t}{q_e} \tag{3}$$

$$\text{Weber's intraparticle diffusion model:} \quad q_t = k_p t^{0.5} + C \tag{4}$$

where q_e (mg g^{-1}) and q_t (mg g^{-1}) are the adsorption capacities at equilibrium and at time t, respectively; k_1

(min^{-1}), k_2 (g mg^{-1} min^{-1}) and k_p (mg g^{-1} $min^{-1/2}$) are rate constants for pseudo-first-order, pseudo-second-order and intraparticle diffusion kinetic models, respectively. C (mg g^{-1}) is the boundary layer constant.

Plots of the adsorption amounts depending on adsorption time and the fitting results through the kinetic models are given in Fig. 5. Adsorption capacity of the $S_{15\%}$-Cu_2O increased rapidly with the prolonged contact time and eventually reached adsorption equilibrium. Table 1 lists the related kinetic parameters obtained by the fitting. Pseudo-second-order kinetic model showed the correlation coefficient $R^2 > 0.99$. The calculated q_e ($q_{e,cal}$) using the pseudo-second-order kinetic model was closer to the experimental q_e ($q_{e,exp}$), which indicated that pseudo-second-order kinetic model was fitted better to describe the adsorption process of MO than pseudo-first-order kinetic model. Pseudo-first-order kinetic model assumes that rate of solute uptake with time is proportional to the difference between saturation concentration and the amount of solid uptake with time, which is generally applicative to the initial adsorption stage. Pseudo-second-order kinetic model predicts the behavior over the whole process of adsorption. In this case, pseudo-second-order kinetic model should give a more appropriate explanation of the adsorption process. It indicates that the adsorption of MO onto S-Cu_2O is an adsorption process involving the electrostatic interaction [20, 47].

Table 1 Kinetic parameters for the adsorption of MO on $S_{15\%}$-Cu_2O

Model	Parameters	Data
Pseudo-first-order model	$q_{e,cal}$ (mg g^{-1})	630.74
	k_1 (min^{-1})	0.0048
	R^2	0.9120
Pseudo-second-order model	$q_{e,cal}$ (mg g^{-1})	1003.40
	k_2 (g mg^{-1} min^{-1})	1.579×10^{-5}
	R^2	0.9989
Intraparticle diffusion model	$k_{i,1}$ (mg g^{-1} $min^{-1/2}$)	47.5912
	R_1^2	0.9986
	$k_{i,2}$ (mg g^{-1} $min^{-1/2}$)	3.8585
	R_2^2	0.8667

Weber's intraparticle diffusion model was applied to describe the rate control steps of the adsorption process [48]. Seen from Fig. 5d, the diffusion step consisted of two sections and the parameters were shown in Table 1. The first portion described the diffusion of MO from bulk solution to the outward surface of the S-Cu_2O adsorbent [35].

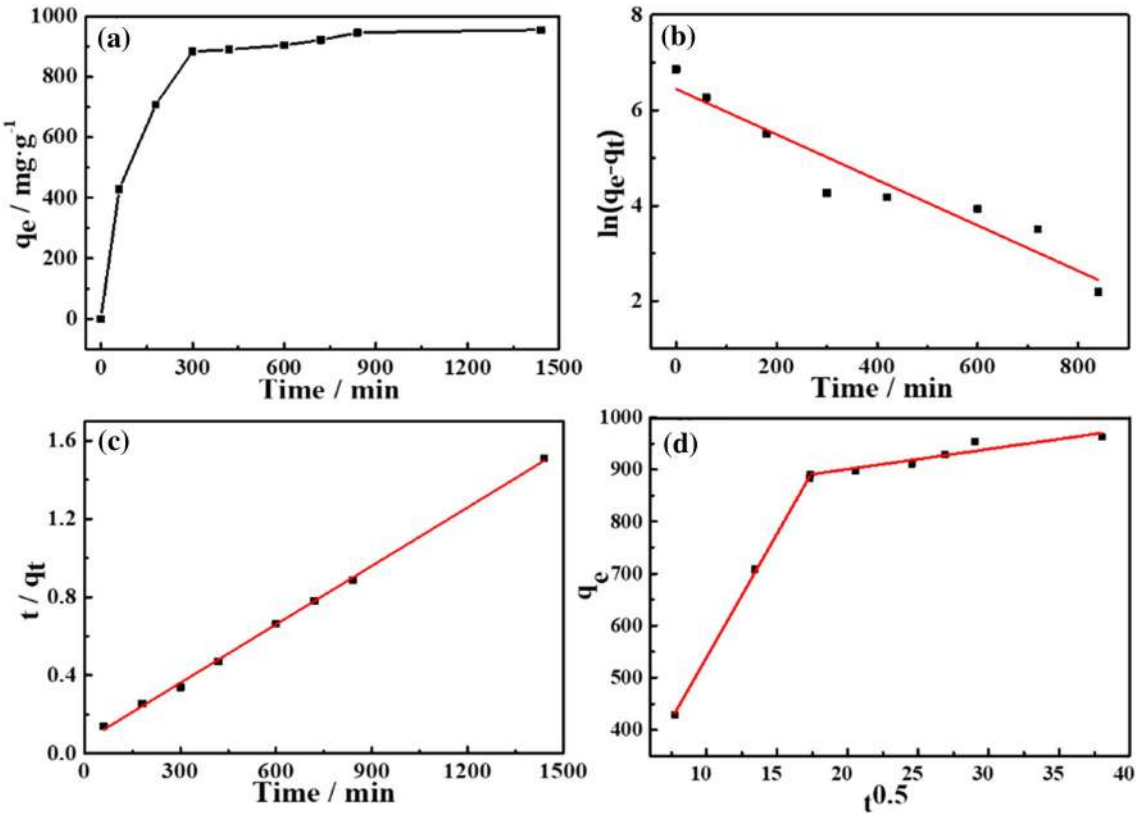

Fig. 5 **a** Relationship between adsorption amount and contacting time; **b** pseudo-first-order kinetic simulation; **c** pseudo-second-order kinetic simulation and **d** Weber's intraparticle diffusion kinetic simulation

While the second region was attributed to the intraparticle diffusion, in which MO molecules moved from the external surface of adsorbent to the active adsorption sites and reached to the final equilibrium stage. As shown in Fig. 5d, the larger slope of the film diffusion stage (k_{i1}) than that of the intraparticle diffusion stage (k_{i2}) indicated the intraparticle diffusion stage was a gradual process, which was consistent with the parameters of Weber's intraparticle diffusion model. The curve did not pass through the origin, which indicated that the intraparticle diffusion was not the sole rate-controlling step in the adsorption process. The intercept of the plot can reflect the boundary layer effect, that is, the larger the intercept, the greater the contribution of the surface adsorption in the rate controlling step [49].

3.4 Adsorption isotherms

For solid–liquid system, adsorption isotherm is an important physico-chemical aspect to describe the relationship between adsorption quantity of adsorbates onto adsorbents and concentration of adsorbates in the aqueous phase at the adsorption equilibriums [7]. To understand adsorption behavior and identify appropriate adsorption isotherm, adsorption experiments of MO with various initial concentrations were conducted on the $S_{15\%}$-Cu_2O adsorbent. Three isotherm models were applied to describe the adsorption of S-Cu_2O, including Langmuir, Freundlich and Dubnin–Radushkevich (D–R) isotherm models. Their relationship equations are presented as follows [50]:

$$\text{Langmuir}: \quad \frac{C_e}{q_e} = \frac{1}{bq_m} + \frac{C_e}{q_m} \tag{5}$$

$$\text{Freundlich}: \quad \ln q_e = \ln K_F + \frac{1}{n} \ln C_e \tag{6}$$

$$\text{D–R}: \ln q_e = \ln q_{D-R} - K_{D-R}\varepsilon^2 \tag{7}$$

where q_m (mg g^{-1}) and q_{D-R} (mg g^{-1}) are the theoretical maximum of adsorption capacity; b (L mg^{-1}) is the Langmuir constant related to adsorption energy; C_e (mg L^{-1}) is the equilibrium concentration in aqueous solution; q_e (mg g^{-1}) is the adsorption capacity at the equilibrium point; K_F [(mg g^{-1}(mg $L^{-1})^{-1/n}$] is the Freundlich constant and n is the adsorption intensity or surface heterogeneity; K_{D-R} (mol^2 J^{-2}) is the D–R constant; ε (J mol^{-1}) is the polanyi potential, which can be calculated by the equation $\varepsilon = RT\ln(1 + 1/C_e)$, where R is the gas constant (8.314 J mol^{-1} K^{-1}); and T (K) is the absolute temperature.

Figure 6a shows the dependence of equilibrium adsorption capacity on the initial concentration of MO. The adsorption capacity of $S_{15\%}$-Cu_2O increased with the incremental initial concentration, and then remained slight change due to saturated occupancy of dye molecules on active adsorption sites of the adsorbent. The fitted plots by Langmuir isotherm and Freundlich isotherm models are shown in Fig. 6b, c. Table 2 gives the corresponding model parameters. The coincidence between the curve and the data points in Fig. 6b is better than that in Fig. 6c. The adsorption capacities fitted by Langmuir isotherm model verged on the experimental values, and the correlation coefficient R^2 (> 0.99) was closer to 1. It suggested that adsorption behavior of S-Cu_2O for MO fitted well with Langmuir isotherm model. The maximum adsorption capacity (q_{max}) of $S_{15\%}$-Cu_2O for MO was calculated to be 1485.24 mg g^{-1}. According to Langmuir isotherm model, the adsorption occurs on a homogenous surface as a monolayer adsorption, in which the adsorption takes place at specific homogeneous site over the coverage surface, and the adsorbed molecules do not interact over the entire adsorption [48]. In the case of Freundlich isotherm model, the adsorption occurs on a heterogeneous surface, which can accommodate more than one molecule at the same location. D–R model predicts the nature of the adsorbate adsorption and it is used to calculate the mean free energy (E, KJ mol^{-1}) of adsorption. The value of E can be calculated by the equation of $E = \frac{1}{\sqrt{2K_{D-R}}}$ [51] and used to determine the type of adsorption either chemical adsorption ($8 < E < 16$ kJ mol^{-1}) or physical adsorption ($E < 8$ kJ mol^{-1}) [52]. The calculated E was 0.0279 kJ mol^{-1}, which demonstrated the adsorption process of the MO by S-Cu_2O was physical adsorption. Furthermore, the values of separation factors (R_L) can characterize the difficulty degree of adsorption reaction system, expressed by the formula $R_L = 1/(1 + K_L C_e)$. Typically, the value of R_L indicates adsorption behavior to be irreversible ($R_L = 0$), favorable ($R_L = 0$–1), linear ($R_L = 1$) and unfavorable ($R_L > 1$) [53]. The value of R_L in this work was between 0 and 1, attesting a favorable adsorption process of MO on S-Cu_2O.

3.5 Thermodynamic analysis

The adsorption thermodynamics was studied to obtain information about the inherent energy change and understand the spontaneity nature of the adsorption. The adsorption experiments were carried out at different temperatures. The thermodynamic parameters including Gibbs free energy change (ΔG^0, KJ mol^{-1}), enthalpy change (ΔS^0, J mol^{-1} K^{-1}) and entropy change (ΔH^0, KJ mol^{-1}) were calculated. ΔH^0 and ΔS^0 of the adsorption process were estimated from Van't Hoff equation [54]. The integrated form of this equation and other related parameters are shown below:

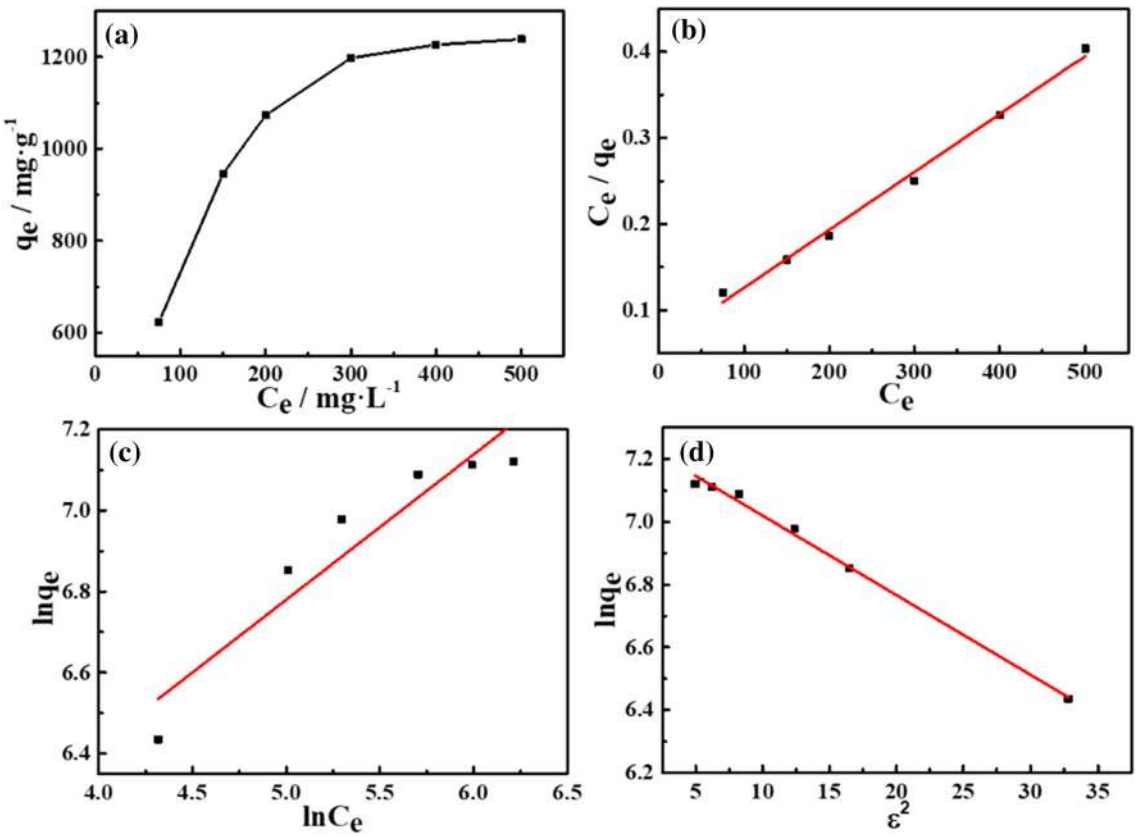

Fig. 6 **a** Relationship between adsorption capacity and initial concentration of MO; **b** Langmuir adsorption isotherm; **c** Freundlich adsorption isotherm and **d** D–R adsorption isotherm

Table 2 Isothermal parameters for the adsorption of MO on $S_{15\%}$-Cu_2O

Model	Parameters	Data
Langmuir	q_m (mg g^{-1})	1485.24
	b (L mg^{-1})	0.0115
	R^2	0.99239
	R_L	0.148–0.537
Freundlich	K_F (mg g^{-1}) (L $mg^{-1})^{1/n}$	148.250
	n	2.804
	R^2	0.86729
D–R	K_{D-R} (mol^2 J^{-2})	0.02534
	q_{D-R} (mg g^{-1})	1443.607
	R^2	0.99404
	E (KJ mol^{-1})	0.0279

$$\ln K_c = -\frac{\Delta H^0}{RT} + \frac{\Delta S^0}{R} \quad (8)$$

$$K_C = \frac{q_e}{C_e} \quad (9)$$

Table 3 Thermodynamic parameters for the adsorption of MO on $S_{15\%}$-Cu_2O

Concentration (mg L^{-1})	ΔH^0 (KJ mol^{-1})	ΔS^0 (J mol^{-1} K^{-1})	$-\Delta G^0$ (KJ mol^{-1})		
			303 K	308 K	313 K
150	−78.4	−235.85	6.51	5.54	4.15

$$\Delta G^0 = -RT \ln K_c \quad (10)$$

where T (K) is the adsorption temperature and R is the universal gas constant. K_C (L g^{-1}) is the thermodynamic equilibrium constant. The relationship of K_C and 1/T is displayed in Fig. S2 and the summarized thermodynamic parameters are given in Table 3. The negative value of ΔG^0 demonstrates that the adsorption process is spontaneous in nature [55]. ΔG^0 values ranging from −20 to 0 kJ mol^{-1} indicate the spontaneous nature of physisorption, whereas the chemisorption involves ΔG^0 values in the range of −80 to −400 kJ mol^{-1} [56]. The calculated ΔG^0 was −6.51, −5.54 and −4.15 kJ mol^{-1} for the adsorption under the three different temperatures. Therefore, the ΔG^0 values suggested that the adsorption of MO onto $S_{15\%}$-Cu_2O was a physical

process, which was consistent with the conclusion derived from the D–R model. The negative value of ΔH^0 confirmed the exothermic characteristic of the adsorption process, suggesting that the adsorption process is more favorable at lower temperature. The negative value of ΔS^0 meant that the adsorption of MO was the transformation from disorder state (random dispersion of MO in the solution) to order state (MO adsorbed on the adsorbent).

3.6 Adsorption mechanism

To know more about the adsorption of MO dye molecules on the S-Cu_2O adsorbent, FT-IR spectra of MO dye before and after adsorption were compared, as shown in Fig. S3. For MO before adsorption, FT-IR spectra in Fig. S3a displayed many peaks indicating the structure of MO. The peaks at 1605 cm^{-1} and 1519 cm^{-1} were from aromatic C=C ring stretching vibration. The peak at 1417 cm^{-1} was classified as N=N stretching vibration. Two peaks detected at 1365 cm^{-1} and 1199 cm^{-1} belonged to the C-N stretching vibration. Amongst these bonds, the N peak at 1365 cm^{-1} connected to aromatic ring while the peak at 1199 cm^{-1} connected to alkyl carbon. The peaks at 1119 cm^{-1}, 1037 cm^{-1} and 696 cm^{-1} were ascribed to the vibrations of sulfonic group. The peak at 1003 cm^{-1} was related to the in-plane bending vibration of C–H. The peaks at 843 cm^{-1} and 817 cm^{-1} resulted from C–H bonds of di-substituted benzene. FT-IR spectra of $S_{15\%}$-Cu_2O (Fig. S3b) were relatively simple. Cu–O bond is located at 624 cm^{-1}. The peak at 1655 cm^{-1} is assigned to –OH bending vibration, which originated from the surface-adsorbed H_2O [28]. In comparison with $S_{15\%}$-Cu_2O, some typical peaks of MO appeared in FT-IR spectra of $S_{15\%}$-Cu_2O after the adsorption of MO (Fig. S3c). It demonstrated the anchored MO molecules onto the surface of S-Cu_2O. FT-IR peaks at 1519 cm^{-1}, 1417 cm^{-1}, 1365 cm^{-1}, 1199 cm^{-1}, 843 cm^{-1} and 817 cm^{-1} occurred obvious changes to be the weakened or vanished peaks. These peaks were from groups located near the center of the aromatic ring of MO, which indicated the adsorption interaction between S-Cu_2O and MO. A possible interaction is n–π interaction which is generally occurred where the lone pair electrons on an oxygen atom are delocalized into the π orbital of an aromatic ring of dye [57]. The presence of oxygen or sulfur elements in S-Cu_2O would provide lone pairs electrons. Clearly, the Cu–O peak decreased significantly in intensity and shifted toward lower wavenumber from 624 to 619 cm^{-1} after the adsorption of MO, which may attribute to n–π electron donor–acceptor interaction between MO and S-Cu_2O [58]. Figure 7 illustrates the possible interaction between MO and S-Cu_2O with electrostatic attractions and n–π interactions. Under the strong alkaline environment, the excessive hydroxyl ions would have a competitive adsorption with the adsorbent, which caused the decreased adsorption amount of MO at high pH as shown in Fig. 4c.

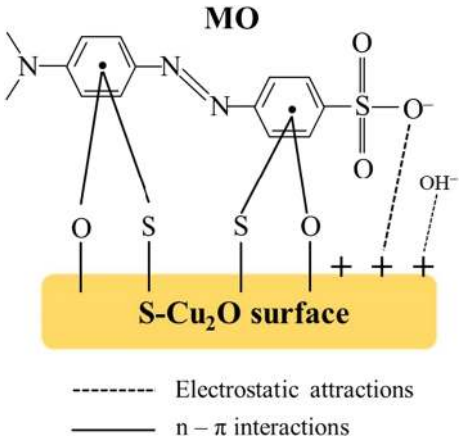

Fig. 7 Illustration of the possible interaction between MO and S-Cu_2O

To understand MO adsorption on the adsorbents surfaces, the electronic properties related to Cu_2O and sulfur incorporated Cu_2O were investigated by density functional theory calculations with coulomb correction (DFT + U), as performed by the VASP. An energy cutoff of 400 eV was adopted for the plane-wave basis. In structural optimizations, the Brillouin zone was sampled by $3 \times 3 \times 1$ k-points using Gamma scheme, while a denser k-points of $9 \times 9 \times 1$ was employed for electronic property computations. A U-J value of 6 eV was used for Cu, which follows the previous calculations on bulk Cu_2O [59]. The energy and force convergence thresholds for the iteration in self-consistent filed (SCF) were set to 10^{-5} eV and 0.02 eV/Å, respectively.

After the full relaxation, the oxygen and sulfur atoms in the surface can coordinate with four nearby copper atoms to form the Cu_4X (X = S or O) moiety (Fig. 8). Bader charge analysis indicated that the copper atoms acts as an electron donor, and about 0.93 and 0.56 |e| are transferred to the surface oxygen/sulfur, respectively. Especially, the charge density difference and the electron localization function (ELF) plots show a pronounced electron accumulation on the sulfur sites. Since the lone pair electrons of oxygen/sulfur in the S-Cu_2O was supposed to form the n–π interaction with MO, these accumulated electrons can strengthen the interactions between the sulfur and MO, leading to the high performance of MO adsorption. Therefore, the promotion effect of the sulfur incorporation is reasonable to be expected, resulting in the higher adsorption capacity of S-Cu_2O than that of pure Cu_2O.

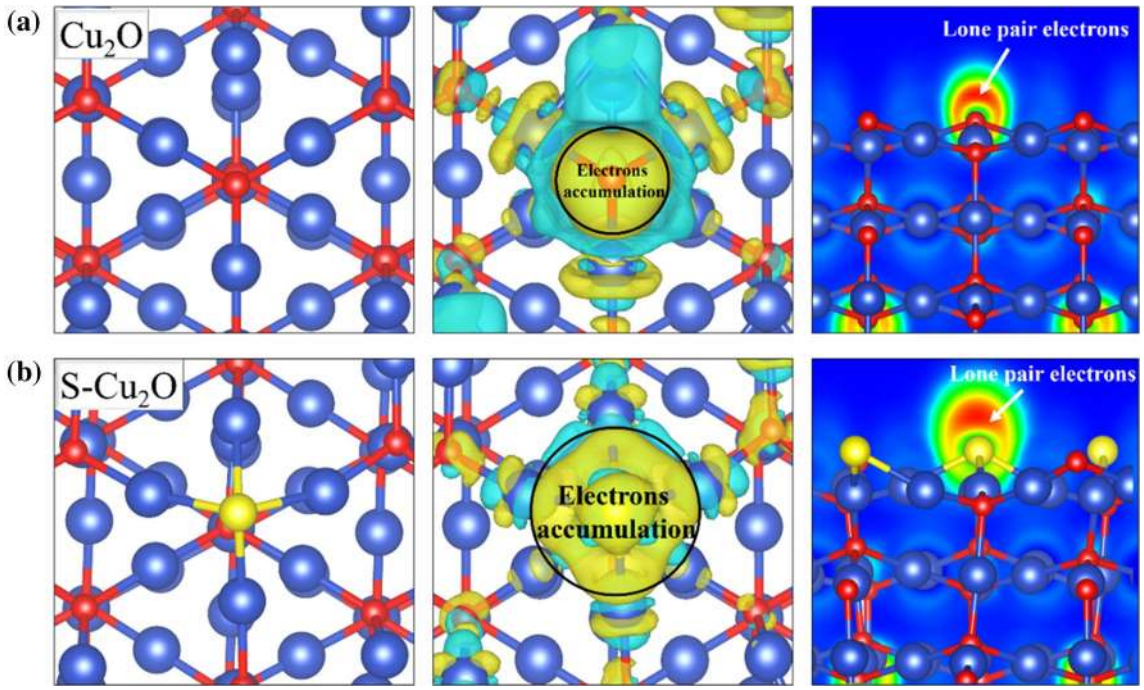

Fig. 8 Optimized structures, charge density differences and electron localization function (ELF) plots of **a** Cu_2O (111) and **b** S-incorporated Cu_2O (111) surfaces (with blue Cu atoms, red O atoms and yellow S atoms). The structures were modelled by 2×2 supercell with five atomic layers, in which the top two layers were fully relaxed while bottom three layers were fixed at their bulk positions

3.7 Selective adsorption ability of S-Cu_2O

Selective adsorption performance of the present $S_{15\%}$-Cu_2O was further investigated in the mixture solution containing both anionic dye and cationic dye. Methylene blue (MB, cationic dye), crystal violet (CV, cationic dye) and methyl orange (MO, anionic dyes) were used as model dyes. All starting concentrations of MO, MB and CV were kept at 50 mg L^{-1} in the adsorption solutions with 10 mg of $S_{15\%}$-Cu_2O adsorbent involved. As observed from Fig. 8, the mixture of MO and MB before adsorption was green color (Fig. 9a) and it turned to blue (Fig. 9b) after adsorption by the adsorbent. The blue color was due to the remaining MB, revealing the adsorption only occurred for the removal of anionic dye MO instead of cationic MB. UV–visible spectra also verified the selective adsorption of S-Cu_2O for MO other than MB (Fig. 9c). As the adsorption ongoing, the intensity of MO at 464 nm decreased obviously with the increasing signal of MB, while the increasing intensity of MB indicated no adsorption of MB on S-Cu_2O. The low intensity of MB at the beginning stage was due to the interference between MO and MB, which was tested by UV–visible spectra of the physical mixture of MO and MB given in Fig. S4. Similarly, the mixtures of MO and CV before and after adsorption gave different colors and the remaining purple solution revealed the existence of cationic dye CV (Fig. 9d, e). UV–visible spectra in Fig. 8f indicated the selective adsorption of anionic dye MO rather cationic dye CV. In a word, the present sulfur-incorporated Cu_2O adsorbent is efficacious in the selective adsorption removal of anionic dyes from cationic dyes containing solution.

Besides the selective adsorption of anionic dye MO, the provided S-Cu_2O adsorbent was efficient for the removal of MO with the promoted adsorption capacity due to the significant effect of sulfur incorporation. The present S-Cu_2O exhibited the predominant adsorption capacity with the higher adsorption amount than most of other adsorbents reported in recent literatures (Table S1). The used S-Cu_2O adsorbents containing MO would be expected for the reuse as adsorbents after calcination to form carbon-containing Cu_2O materials in our further researches. The sulfur-incorporated Cu_2O adsorbents synthesized through the facile method in this work would provide their potential applications for the removal organic dye pollutants.

4 Conclusions

Nonmetallic sulfur element was incorporated into Cu_2O to form S-Cu_2O nanocomposites through a facile chemical liquid phase reduction method. Homogeneous cubic S-Cu_2O nanoparticles were obtained. X-ray powder diffraction patterns indicated the sulfur incorporation into crystal

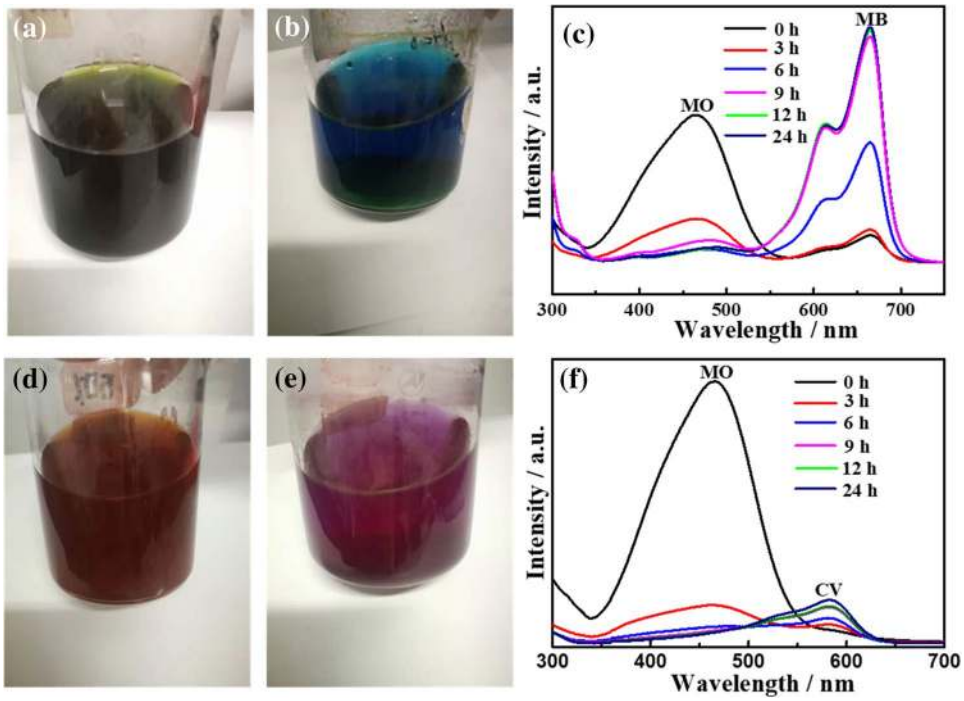

Fig. 9 Photos of the mixture of MO and MB **a** before adsorption and **b** after adsorption; Photos of the mixture of MO and CV **d** before adsorption and **e** after adsorption; UV–visible spectra of **c** MO/MB and **f** MO/CV mixture solutions during the adsorption reaction on the $S_{15\%}$-Cu_2O adsorbent

lattice oxygen. The participation of sulfur precursor TAA resulted in the obvious decrease of particles sizes from 1.5 μm (Cu_2O) to 50 nm (S-Cu_2O). The $S_{15\%}$-Cu_2O nanomaterial, synthesized with the molar percentage of TAA to $CuCl_2$ as 15%, showed outstanding adsorption performance with a maximum adsorption capacity (q_{max}) of 1485.24 mg g^{-1} for MO, which was much higher than Cu_2O. Kinetic studies indicated that the adsorption process followed the pseudo-second-order kinetic model. The equilibrium data fitted the Langmuir isotherm model well and the D–R model stated that the adsorption was a physical process. Thermodynamic studies suggested the exothermic and spontaneous adsorption process. The S-Cu_2O adsorbent has good selective adsorption ability for anionic dye MO from other cationic dyes. Density functional theory calculations proved a pronounced electron accumulation on sulfur sites, strengthening the interactions between S-Cu_2O and MO, which led to the high adsorption performance of S-Cu_2O for MO. This work provided a promising strategy of nonmetallic incorporation for improving adsorption capacity of other metal oxide adsorbents.

Funding This study was funded by the National Natural Science Foundation of China (21106006).

Compliance with ethical standards

Conflict of interest The authors declare that they have no conflict of interest.

References

1. Valley B, Jing B, Ferreira M, Zhu Y (2019) Rapid and efficient coacervate extraction of cationic industrial dyes from wastewater. ACS Appl Mater Interfaces 11:7472–7478. https://doi.org/10.1021/acsami.8b21674
2. Wu Y, Su M, Chen J, Xu Z, Tang J, Chang X, Chen D (2019) Superior adsorption of methyl orange by h-MoS_2 microspheres: isotherm, kinetics, and thermodynamic studies. Dyes Pigments 170:107591. https://doi.org/10.1016/j.dyepig.2019.107591
3. Fan M, Wang Y, Wang Z, Zhao Y, Gao B, Chu Y, Zhou W, Yan C (2019) Transformation of silver nanoparticles in coagulation processes and subsequent thermal sludge treatments. J Clean Prod 238:117984. https://doi.org/10.1016/j.jclepro.2019.117984
4. Zhan Y, Wan X, He Yang Q, He Y (2018) Design of durable and efficient poly(arylene ether nitrile)/bioinspired polydopamine coated graphene oxide nanofibrous composite membrane for anionic dyes separation. Chem Eng J 333:132–145. https://doi.org/10.1016/j.cej.2017.09.147
5. Li X, Shi JL, Hao H, Lang X (2018) Visible light-induced selective oxidation of alcohols with air by dye-sensitized TiO_2 photocatalysis. Appl Catal B Environ 232:260–267. https://doi.org/10.1016/j.apcatb.2018.03.043
6. Yousefi M, Villar-Rodil S, Paredes JI, Moshfegh AZ (2019) Oxidized graphitic carbon nitride nanosheets as an effective adsorbent for organic dyes and tetracycline for water remediation. J Alloy Compd 809:151783. https://doi.org/10.1016/j.jallcom.2019.151783
7. Zheng Y, Cheng B, You W, Yu J, Ho W (2019) 3D hierarchical graphene oxide-NiFe LDH composite with enhanced adsorption affinity to Congo red, methyl orange and Cr(VI) ions. J Hazard Mater 369:214–225. https://doi.org/10.1016/j.jhazmat.2019.02.013
8. Wu Z, Zhang H, Luo L, Tu W (2019) ZnCo binary hydroxide nanostructures for the efficient removal of cationic dyes. J

Alloy Compd 806:823–832. https://doi.org/10.1016/j.jallcom.2019.07.295
9. Jawad AH, Abdulhameed AS (2020) Mesoporous Iraqi red kaolin clay as an efficient adsorbent for methylene blue dye: adsorption kinetic, isotherm and mechanism study. Surf Interfaces 18:100422. https://doi.org/10.1016/j.surfin.2019.100422
10. Jawad AH, Abdulhameed AS, Mastuli MS (2020) Mesoporous crosslinked chitosan-activated charcoal composite for the removal of thionine cationic dye: comprehensive adsorption and mechanism study. J Polym Environ 28:1095–1105. https://doi.org/10.1007/s10924-020-01671-5
11. Abdulhameed AS, Mohammad AT, Jawad AH (2019) Modeling and mechanism of reactive orange 16 dye adsorption by chitosan-glyoxal/TiO_2 nanocomposite: application of response surface methodology. Desalin Water Treat 164:346–360. https://doi.org/10.5004/dwt.2019.24384
12. Jawad AH, Abdulhameed AS, Mastuli MS (2020) Acid-factionalized biomass material for methylene blue dye removal: a comprehensive adsorption and mechanism study. J Taibah Univ Sci 14:305–313. https://doi.org/10.1080/16583655.2020.1736767
13. Jawad AH, Mubarak NSA, Abdulhameed AS (2020) Tunable Schiff's base-cross-linked chitosan composite for the removal of reactive red 120 dye: adsorption and mechanism study. Int J Biol Macromol 142:732–741. https://doi.org/10.1016/j.ijbiomac.2019.10.014
14. Malek NNA, Jawad AH, Abdulhameed AS, Ismail K, Hameed BH (2020) New magnetic Schiff's base-chitosan-glyoxal/fly ash/Fe_3O_4 biocomposite for the removal of anionic azo dye: an optimized process. Int J Biol Macromol 146:530–539. https://doi.org/10.1016/j.ijbiomac.2020.01.020
15. Jawad AH, Abdulhameed AS, Mohammad AT (2019) Application of response surface methodology for enhanced synthesis of chitosan tripolyphosphate/TiO_2 nanocomposite and adsorption of reactive orange 16 dye. J Clean Prod 232:43–56. https://doi.org/10.1016/j.jclepro.2019.05.291
16. Jawad AH, Mubarak NSA, Abdulhameed AS (2019) Hybrid crosslinked chitosan-epichlorohydrin/TiO_2 nanocomposite for reactive red 120 dye adsorption: kinetic, isotherm, thermodynamic, and mechanism study. J Polym Environ 28:624–637. https://doi.org/10.1007/s10924-019-01631-8
17. Zayed AM, Abdel Wahed MSM, Mohamed EA, Sillanpää M (2018) Insights on the role of organic matters of some Egyptian clays in methyl orange adsorption: isotherm and kinetic studies. Appl Clay Sci 166:49–60. https://doi.org/10.1016/j.clay.2018.09.013
18. Labiadh L, Kamali AR (2019) 3D graphene nanoedges as efficient dye adsorbents with ultra-high thermal regeneration performance. Appl Surf Sci 490:383–394. https://doi.org/10.1016/j.apsusc.2019.06.081
19. Wang B, Yang X, Ma L, Zhai L, Xuan J, Liu C, Bai Z (2020) Ultra-high efficient pH induced selective removal of cationic and anionic dyes from complex coexisted solution by novel amphoteric biocomposite microspheres. Sep Purif Technol 231:115922. https://doi.org/10.1016/j.seppur.2019.115922
20. Deb A, Kanmani M, Debnath A, Bhowmik KL, Saha B (2019) Ultrasonic assisted enhanced adsorption of methyl orange dye onto polyaniline impregnated zinc oxide nanoparticles: kinetic, isotherm and optimization of process parameters. Ultrason Sonochem 54:290–301. https://doi.org/10.1016/j.ultsonch.2019.01.028
21. Deb A, Kanmani M, Debnath A, Saha B (2019) Ultrasound-aided rapid and enhanced adsorption of anionic dyes from binary dye matrix onto novel hematite/polyaniline nanocomposite: response surface methodology optimization. Appl Organomet Chem 34:e5353. https://doi.org/10.1002/aoc.5353
22. Bhowmik KL, Deb K, Bera A, Debnath A, Saha B (2018) Interaction of anionic dyes with polyaniline implanted cellulose: organic π-conjugated macromolecules in environmental applications. J Mol Liq 261:189–198. https://doi.org/10.1016/j.molliq.2018.03.128
23. Grover A, Mohiuddin I, Malik AK, Aulakh JS, Kim KH (2019) Zn-Al layered double hydroxides intercalated with surfactant: synthesis and applications for efficient removal of organic dyes. J Clean Prod 240:118090. https://doi.org/10.1016/j.jclepro.2019.118090
24. Iman K, Shahid M, Khan MS, Ahmad M, Sama F (2019) Topology, magnetism and dye adsorption properties of metal organic frameworks (MOFs) synthesized from bench chemicals. CrystEngComm 21:5299–5309. https://doi.org/10.1039/c9ce01041f
25. Zafar MN, Dar Q, Nawaz F, Zafar MN, Iqbal M, Nazar MF (2019) Effective adsorptive removal of azo dyes over spherical ZnO nanoparticles. J Mater Res Technol 8:713–725. https://doi.org/10.1016/j.jmrt.2018.06.002
26. Bhowmik M, Deb K, Debnath A, Saha B (2017) Mixed phase Fe_2O_3/Mn_3O_4 magnetic nanocomposite for enhanced adsorption of methyl orange dye: neural network modeling and response surface methodology optimization. Appl Organomet Chem 32:e4186. https://doi.org/10.1002/aoc.4186
27. Bhowmik KL, Debnath A, Nath RK, Das S, Chattopadhyay KK, Saha B (2016) Synthesis and characterization of mixed phase manganese ferrite and hausmannite magnetic nanoparticle as potential adsorbent for methyl orange from aqueous media: artificial neural network modeling. J Mol Liq 219:1010–1022. https://doi.org/10.1016/j.molliq.2016.04.009
28. Zhang Y, Wang D, Zhang X, Qu F (2013) Template-free synthesis of porous Cu_2O nanospheres at room temperature and investigation on their adsorption property. J Nanomater 2013:1–5. https://doi.org/10.1155/2013/378919
29. Ho WCJ, Tay Q, Qi H, Huang Z, Li J, Chen Z (2017) Photocatalytic and adsorption performances of faceted cuprous oxide (Cu_2O) particles for the removal of methyl orange (MO) from aqueous media. Molecules 22:677. https://doi.org/10.3390/molecules22040677
30. Xu Y, Liu P, Cao Y, Sun Y, Zhang G (2016) Room-temperature synthesis of Cu_2O nanostructures and their morphology-dependent adsorption properties. B Korean Chem Soc 37:1114–1123. https://doi.org/10.1002/bkcs.10834
31. Jing HY, Wen T, Fan CM, Gao GQ, Zhong SL, Xu AW (2014) Efficient adsorption/photodegradation of organic pollutants from aqueous systems using Cu_2O nanocrystals as a novel integrated photocatalytic adsorbent. J Mater Chem A 2:14563–14570. https://doi.org/10.1039/c4ta02459a
32. Kou T, Wang Y, Zhang C, Sun J, Zhang Z (2013) Adsorption behavior of methyl orange onto nanoporous core–shell Cu@Cu_2O nanocomposite. Chem Eng J 223:76–83. https://doi.org/10.1016/j.cej.2013.03.013
33. Sasmal AK, Pal J, Sahoo R, Kartikeya P, Dutta S, Pal T (2016) Superb dye adsorption and dye-sensitized change in Cu_2O–Ag crystal faces in the dark. J Phys Chem C 120:21580–21588. https://doi.org/10.1021/acs.jpcc.6b07300
34. Tang H, Yang W, Fu L, Zhu J, Li D, Zhou L (2019) Excellent adsorption capacity and photocatalytic regeneration of nanoparticles-assembled mesoporous Cu_2O/Bi_2O_3 composites for removal of methyl orange. Mater Res Express 6:085532. https://doi.org/10.1088/2053-1591/ab2439
35. Wang Y, Ghanbaja J, Horwat D, Yu L, Pierson JF (2017) Nitrogen chemical state in N-incorporated Cu_2O thin films. Appl Phys Lett 110:131902. https://doi.org/10.1063/1.4979140
36. Navaee A, Salimi A (2017) Sulfur incorporated-copper oxide nanoclusters synthesized through a facile electroplating process assisted by thiourea for selective photoelectrocatalytic reduction of CO_2. J Colloid Interface Sci 505:241–252. https://doi.org/10.1016/j.jcis.2017.05.103

37. Shah AA, Ahmad S, Azam A (2020) Investigation of structural, optical, dielectric and magnetic properties of $LaNiO_3$ and $LaNi_{1-x}M_xO_3$ (M = Fe, Cr & Co; x = 5%) nanoparticles. J Magn Magn Mater 494:165812. https://doi.org/10.1016/j.jmmm.2019.165812
38. Abdi M, Mahdikhah V, Sheibani S (2020) Visible light photocatalytic performance of La–Fe co-doped $SrTiO_3$ perovskite powder. Opt Mater 102:109803. https://doi.org/10.1016/j.optmat.2020.109803
39. Elmehasseb I, Kandil S, Elgendy K (2020) Advanced visible-light applications utilizing modified Zn-doped TiO_2 nanoparticles via non-metal in situ dual doping for wastewater detoxification. Optik. https://doi.org/10.1016/j.ijleo.2020.164654
40. Liu SH, Lu JS (2018) Facet-dependent cuprous oxide nanocrystals decorated with graphene as durable photocatalysts under visible light. Nanomaterials 8:423. https://doi.org/10.3390/nano8060423
41. Liao H, Wang Z (2018) Adsorption removal of amaranth by nanoparticles-composed Cu_2O microspheres. J Alloy Compd 769:1088–1095. https://doi.org/10.1016/j.jallcom.2018.08.088
42. Liu F, Liu Q, Liu Y, Xue RT, Li P, Fan XM (2019) Synthesis and photocatalytic activity of cubic cuprous oxide supported on activated carbon fibers. Chem Phys Lett 718:54–62. https://doi.org/10.1016/j.cplett.2019.01.011
43. Pang J, Li W, Cao Z, Xu J, Li X, Zhang X (2018) Mesoporous Cu_2O–CeO_2 composite nanospheres with enhanced catalytic activity for 4-nitrophenol reduction. Appl Surf Sci 439:420–429. https://doi.org/10.1016/j.apsusc.2018.01.055
44. Yu X, Yu ZY, Zhang XL, Li P, Sun B, Gao X, Yan K, Liu H, Duan Y, Gao MR, Wang G, Yu SH (2020) Highly disordered cobalt oxide nanostructure induced by sulfur incorporation for efficient overall water splitting. Nano Energy 71:104652. https://doi.org/10.1016/j.nanoen.2020.104652
45. Liu J, Gao Z, Han H, Wu D, Xu F, Wang H, Jiang K (2012) Mesoporous Cu_2O submicro-spheres, facile synthesis and the selective adsorption properties. Chem Eng J 185–186:151–159. https://doi.org/10.1016/j.cej.2012.01.064
46. Hu H, Liu J, Xu Z, Zhang L, Cheng B, Ho W (2019) Hierarchical porous Ni/Co-LDH hollow dodecahedron with excellent adsorption property for Congo red and Cr(VI) ions. Appl Surf Sci 478:981–990. https://doi.org/10.1016/j.apsusc.2019.02.008
47. Jawad AH, Malek NNA, Abdulhameed AS, Razuan R (2020) Synthesis of magnetic chitosan-fly ash/Fe_3O_4 composite for adsorption of reactive orange 16 dye: optimization by Box–Behnken design. J Polym Environ 28:1068–1082. https://doi.org/10.1007/s10924-020-01669-z
48. Cheng L, Hou C, Zhang B, Liu G (2016) Synthesis, characterization of nitrogen-incorporated mesoporous carbon spheres and adsorption performance. RSC Adv 6:114361–114373. https://doi.org/10.1039/c6ra23631f
49. Fu J, Zhu J, Wang Z, Wang Y, Wang S, Yan R, Xu Q (2019) Highly-efficient and selective adsorption of anionic dyes onto hollow polymer microcapsules having a high surface-density of amino groups: isotherms, kinetics, thermodynamics and mechanism. J Colloid Interface Sci 542:123–135. https://doi.org/10.1016/j.jcis.2019.01.131
50. Ibrahim RK, El-Shafie A, Hin LS, Mohd NSB, Aljumaily MM, Ibraim S, AlSaadi MA (2019) A clean approach for functionalized carbon nanotubes by deep eutectic solvents and their performance in the adsorption of methyl orange from aqueous solution. J Environ Manag 235:521–534. https://doi.org/10.1016/j.jenvman.2019.01.070
51. Kara A, Demirbel E, Tekin N, Osman B, Besirli N (2015) Magnetic vinylphenyl boronic acid microparticles for Cr(VI) adsorption: kinetic, isotherm and thermodynamic studies. J Hazard Mater 286:612–623. https://doi.org/10.1016/j.jhazmat.2014.12.011
52. Unlu N, Ersoz M (2006) Adsorption characteristics of heavy metal ions onto a low cost biopolymeric sorbent from aqueous solutions. J Hazard Mater 136:272–280. https://doi.org/10.1016/j.jhazmat.2005.12.013
53. Darwish AAA, Rashad M, Al-Aoh HA (2019) Methyl orange adsorption comparison on nanoparticles: isotherm, kinetics, and thermodynamic studies. Dyes Pigments 160:563–571. https://doi.org/10.1016/j.dyepig.2018.08.045
54. Shu J, Wang Z, Huang Y, Huang N, Ren C, Zhang W (2015) Adsorption removal of Congo red from aqueous solution by polyhedral Cu_2O nanoparticles: kinetics, isotherms, thermodynamics and mechanism analysis. J Alloy Compd 633:338–346. https://doi.org/10.1016/j.jallcom.2015.02.048
55. Liu Y, Tian Y, Luo C, Cui G, Yan S (2015) One-pot preparation of a MnO_2–graphene–carbon nanotube hybrid material for the removal of methyl orange from aqueous solutions. New J Chem 39:5484–5492. https://doi.org/10.1039/c5nj00697j
56. Han J, Jun BM, Heo J, Lee G, Yoon Y, Park CM (2019) Highly efficient organic dye removal from waters by magnetically recoverable $La_2O_2CO_3$/$ZnFe_2O_4$-reduced graphene oxide nanohybrid. Ceram Int 45:19247–19256. https://doi.org/10.1016/j.ceramint.2019.06.173
57. Mohammad AT, Abdulhameed AS, Jawad AH (2019) Box–Behnken design to optimize the synthesis of new crosslinked chitosan-glyoxal/TiO_2 nanocomposite: methyl orange adsorption and mechanism studies. Int J Biol Macromol 129:98–109. https://doi.org/10.1016/j.ijbiomac.2019.02.025
58. Tran HN, You SJ, Chao HP (2017) Insight into adsorption mechanism of cationic dye onto agricultural residues-derived hydrochars: negligible role of π–π interaction. Korean J Chem Eng 34:1708–1720. https://doi.org/10.1007/s11814-017-0056-7
59. Bendavid LI, Carter EA (2013) CO_2 adsorption on Cu_2O(111): a DFT+U and DFT-D study. J Phys Chem C 117:26048–26059. https://doi.org/10.1021/jp407468t